Geophysical Journal International

Geophys. J. Int. (2014) **198,** 504–515
Advance Access publication 2014 May 27
GJI Seismology

doi: 10.1093/gji/ggu148

Frequency-dependent seismic attenuation in shales: experimental results and theoretical analysis

Claudio Delle Piane,[1] Joel Sarout,[1] Claudio Madonna,[2] Erik H. Saenger,[2] David N. Dewhurst[1] and Mark Raven[3]

[1] *CSIRO Earth Science and Resource Engineering, Australian Resources Research Centre, 26 Dick Perry Avenue, Kensington, WA 6151, Australia. E-mail: claudio.dellepiane@csiro.au*
[2] *Geological Department ETH, Sonneggstrasse 5, CH-8092 Zurich, Switzerland*
[3] *CSIRO Land and Water, Waite Rd, Urrbrae, SA 5064, Australia*

Accepted 2014 April 17. Received 2014 February 2; in original form 2013 August 2

SUMMARY

Samples of shales from the Ordovician Bongabinni and Goldwyer source rock formations were recovered from the Canning Basin (Western Australia). Attenuation was experimentally measured on preserved plugs from these formations in the frequency range between 10^{-2} and 10^{2} Hz. Samples cored with different orientations with respect to the sedimentary bedding were prepared and tested in their native saturated state and after drying in the oven at 105 °C for 24 hr to assess the effect of fluids and of the sediment anisotropy on attenuation. To aid the interpretation of the experimental results, the clay-rich samples were characterized in terms of mineralogy, water content, porosity, permeability and microstructure.

The two shales have significantly different quality factors; and this is seen to be dependent on both the saturation state of the samples and the propagation direction of the oscillatory signal. The attenuation coefficient for compression/extension parallel to bedding is less than that vertical to bedding in both the preserved and partially dehydrated situations.

No frequency dependency is observed in the preserved samples within the range of frequencies explored in this study. On the other hand partially saturated samples show peaks in attenuation at around 40 Hz when the stress perturbation is transmitted normal to the macroscopic bedding. The interpretation of the attenuation measurements in terms of well-established theoretical models is discussed in view of the physical characteristics and microstructure of the tested rocks.

Key words: Seismic anisotropy; Seismic attenuation; Wave propagation.

1 INTRODUCTION

Seismic wave attenuation is an anelastic phenomenon that is responsible for dissipation of the mechanical energy during the propagation of the wave through a body of rocks. It results in the decay of amplitude of the seismic wave. From a geophysical perspective, understanding attenuation in rocks is of paramount importance as most of the information available on the structure, composition and organization of the earth below the surface is gathered from seismic waves. Global geodynamic models are constrained by the attenuation of teleseismic waves (e.g. Carpenter & Flinn 1965). On the other hand, interactions between the rock frame and the possible pore fluids can induce attenuation, which in turn might be detected by borehole/exploration geophysics tools providing important insights into the fluid content and type in shallow porous rock bodies (e.g. Klimentos 1995).

In porous rocks attenuation is generally associated with the presence of fluids in the pore network; moreover the capacity of fluids to move as a consequence of transient stress perturbation induces frequency dependency in the attenuation (Winkler & Murphy 1995; Muller *et al.* 2010; Sarout 2012). Broad frequency measurements are therefore needed to reconcile laboratory ultrasonic measurements (∼MHz range) and borehole (∼tens of kHz) and exploration (∼10–100 Hz) geophysics. It should be noted that dispersion and attenuation at these frequencies is typically ignored in field seismic applications partly due to the lack of experimental data. The results of low frequency laboratory tests are therefore relevant for applications like traditional Amplitude Versus Offset (AVO, Allen & Petty 1993) analysis.

Experimental studies on low frequency attenuation of rocks have been reported since the 1980s (e.g. Spencer 1981; Murphy 1982; Winkler & Nur 1982). They indicated the importance of the

pore-saturating fluids in inducing a frequency dependent seismic response of the rock. Such behaviour contrasts with the case of a vacuum-dried rock for which a negligible dependency of the seismic response on frequency was observed.

Batzle *et al.* (2006) explained such behaviour in terms of fluid mobility M defined as the ratio of rock permeability on fluid viscosity and pore pressure distribution within porous rocks: lowering fluid mobility (by low rock permeability, or by high fluid viscosity) increases the relaxation time required to equilibrate the pore pressure altered by a passing wave within a rock. Consequently, under conditions where the period of the elastic perturbation is shorter than the fluid relaxation time, the fluid saturated rock will appear stiffer than at lower frequencies.

Experimental evidence to support this thesis has been provided for sandstones (Batzle *et al.* 2006) and carbonates (Adam *et al.* 2006). Recently Adelinet *et al.* (2010) also reported a comparison of low and high frequency elastic moduli measured on basalt samples and explained their difference through a combination of local viscous flow (squirt flow) of pore fluid between compliant and stiff pores and chemical interactions between the pore fluid and the rock frame.

Experiments aimed at measuring frequency dependant attenuation on shales are strikingly rare: Hofmann (2006) reported measurements on two types of shales with contrasting behaviour which was qualitatively attributed to their different pore space arrangement. Sarker & Batzle (2010) also performed tests on samples of dry and decane-saturated Mancos shale observing negligible frequency dependence of the anisotropic elastic moduli on frequency between 0.2 and 1000 Hz.

This paper reports results of direct measurements of attenuation in the frequency range 0.1–100 Hz, on shale samples extracted from an onshore well in Western Australia. The samples belonging to two distinct geological formations, are first characterized in terms of mineralogy, microstructure and porosity and permeability, and then tested at room conditions to measure their attenuation firstly in their preserved state and secondly in a partially saturated state after drying in an oven for 24 hr at 105 °C. Where possible, orthogonally oriented specimens have been tested to also assess the anisotropy of attenuation.

These experiments indicate that attenuation is frequency dependent and is higher in the partially saturated than in the preserved state. It is also shown that attenuation has an anisotropic expression and is higher for simulated wave propagation perpendicular to the shale bedding plane then parallel to it. The experimental results are interpreted in the light of well-established attenuation theories and an attempt is made to invert the data in terms of rock microstructural parameters. The magnitude of these parameters is found to be consistent with classical results on rock microstructures.

2 SAMPLE PROVENANCE

The shales specimen used in this study are sampled from an onshore well drilled in the Canning Basin (Western Australia). The geothermal history and depth of burial constrained by apatite fission track and vitrinite reflectance analyses, indicate that the sediment reached the maximum burial depth of approximately 5000 m in the Early Jurassic and witnessed maximum temperatures of 160–180 °C (Ghori & Haines 2006).

The Middle Ordovician Goldwyer Formation is mainly of open marine to intertidal origin (Haines 2004), while the Bongabinni Formation is mostly an oxidised marginal marine to supratidal deposit.

The fine-grained nature of shales and their characteristic physico- and electrochemistry necessitate the use of special techniques to ensure that samples are tested in as close to a representative state as possible. This requires therefore that precautions are taken to avoid desiccation of shales after coring to avoid fracturing of the shale, inducing large capillary stresses and changes of strength, particle orientation and pore size distribution.

The parent shale cores were extracted from depths ranging between 1505 and 1852 meters (i.e. significantly shallower than their estimated maximum burial depth) and preserved under oil in a sealed PVC core liner to maintain their native water content. Subsamples for attenuation and permeability testing, were plugged and trimmed using oil as a drilling fluid and stored under light process oil to prevent evaporation of pore fluids. Offcuts from these samples were used for sample characterisation in terms of grain size distribution, pore size distribution, porosity, composition, grain density and microstructural evaluation. These samples were similarly stored and preserved under oil until tested.

3 EXPERIMENTAL METHODS

3.1 General characterization

Computed tomography (CT) images corresponding to a 2-D linear X-ray attenuation pixel matrix were acquired with a Toshiba medical imager. The whole core section, still sealed in its plastic liner, was first screened by passing through the X-ray apparatus in scanogram mode, producing a projection radiograph. This showed the bedding orientation and the presence of fractures. The core plug sample positions and orientations were selected based on these preliminary observations. Once cored, the specimens were stored in a glass jar filled with mineral oil and scanned again to visualise any additional internal features possibly present in each specimen.

Quantitative mineralogy analysis of each sample was performed through X-ray powder diffraction (XRD) using the same procedures and sample preparation described in Delle Piane *et al.* (2011a).

The XRD patterns were recorded with a PANalytical X'Pert Pro multipurpose X-ray diffractometer using iron-filtered Cobalt Kα radiation. The diffraction patterns were recorded in steps of $2\theta = 0.017^{\circ}$ with a 0.5 s counting time per step, and logged to data files for further processing and analysis. Quantitative analysis was performed on the XRD data using the commercial package SIRO-QUANT from Sietronics Pty Ltd. The results are normalised to 100 per cent and hence do not include unidentified or amorphous materials.

Results of the XRD analysis are used to calculate the clay content (CC) and clay fraction (CF) of the shale defined as follows

$$CF = \text{wt\%} < 2\,\mu\text{m fraction} \tag{1}$$

$$CC = \sum \text{wt\% clay minerals.} \tag{2}$$

Interconnected porosity and pore-size distribution of the samples was quantified by mercury injection porosimetry using a Micromeritics Autopore III. This equipment is capable of injecting mercury at user-defined pressure increments up to 60 000 psi (~413 MPa) into a dry and porous rock sample. Cubic samples were resin-coated on four faces such that mercury was forced to intrude through two opposite faces of the cube, normal to the shale bedding plane.

The determination of the pore size distribution assumes that the rock is made of a bundle of parallel capillary tubes with different

radii. Following Jurin (1719), the capillary pressure *Pc* in a circular tube of radius r is given by

$$P_C = \frac{2\gamma \cos\theta}{r} \tag{3}$$

where γ is the mercury-air surface tension and θ is the contact angle between the mercury and the solid phase (140°).

Water content of the shales was measured as well by weighing a chunk of preserved rock in its (assumed) saturated state (wt_w), followed by drying in a vacuum oven at 105 °C and remeasuring of the dry weight (wt_d). Water content (w) is then given by

$$w = \frac{wt_w - wt_d}{wt_d} \times 100. \tag{4}$$

For an evaluation of the drying stage of the shale samples, their weights were monitored as a function of time at constant temperature in the oven. Each weight measurement was taken after the sample cooled down under vacuum to room temperature. Following Ghorbani *et al.* (2009), the characteristic time (τ) required to reach thermal equilibrium is estimated as

$$\tau = \frac{L^2 c}{\lambda}, \tag{5}$$

where L is the thermal diffusion characteristic length of the sample; c is the volumetric heat capacity and λ is the thermal conductivity. Approximately 2 hr are needed at room conditions for the sample to cool down if one considers $L \approx 0.01$ m; $c \approx 2 \times 10^6$ J m^{-3} K^{-1} and $\lambda \approx 1.5$ W m^{-1} K^{-1} (Ghorbani *et al.* 2009 and references therein). After the weight measurement at these conditions the samples are placed back in the oven until the next reading is taken with the same procedure.

This procedure also allowed for the estimation of the saturation state of the sample at each step, assuming that each sample was initially fully saturated. The saturation state (S_w) at each drying stage is calculated as

$$S_w = \frac{\phi - w_v}{\phi}, \tag{6}$$

where ϕ and (w_v) are the total volumetric fractions of interconnected porosity and water content, respectively.

3.2 Permeability measurements

The membrane efficiency screening equipment was used for the experimental determination of the permeability of shale specimens using the steady-state flow method (Brace 1980; Neuzil 1994; Jones & Meredith 1998; Boisson *et al.* 2001). The choice of this method for measuring permeability is dictated by its reliability since it does not require any data processing such as model inversion; neither is it influenced by the specific experimental setup used to perform the measurement (e.g. downstream dead volume).

The specimens were prepared to the following dimensions: length $L \sim 12$ mm and diameter $D \sim 25$ mm. The flow of fluid during the test occurred over the length of the cylindrical sample, characterizing therefore the permeability at the centimetre scale. During the test, confining pressure was maintained constant at $P_C = 20$ MPa. The tests were performed at room temperature, generally with observed variations less than ±0.5 °C over the course of the test (few weeks). The preliminary resaturation and further permeability testing of the shale samples was performed with a simulated pore fluid with 3.5 wt% of sodium chloride simulating average sea water composition. Such choice was made in consideration of the original

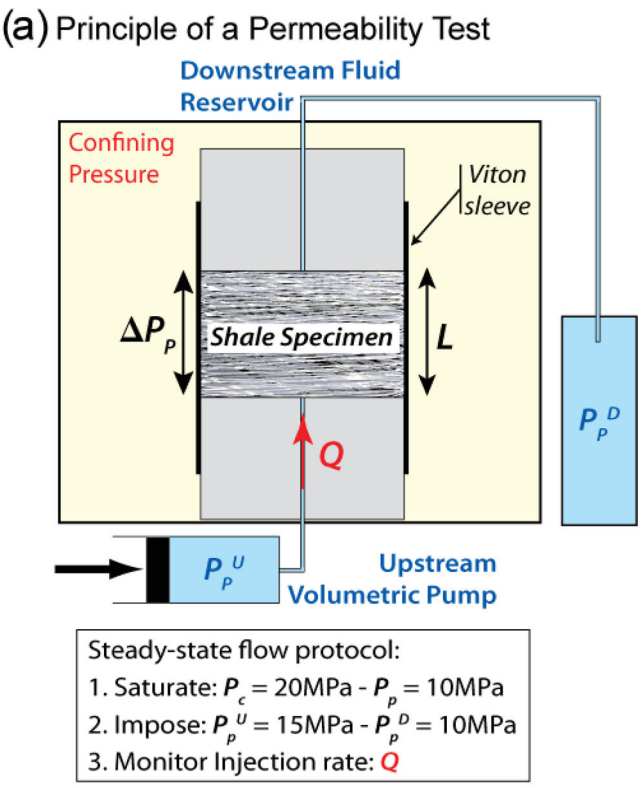

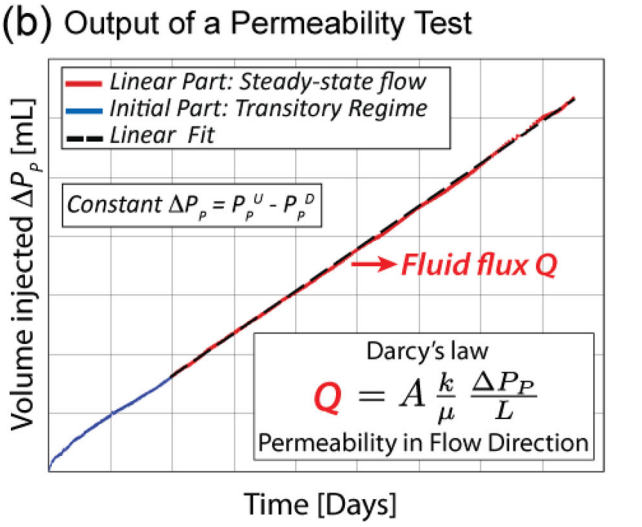

Figure 1. (a) Schematic illustration of the experimental setup allowing for the measurement of the water permeability of a shale sample using the steady-state flow method. (b) Typical output dataset of a permeability test were the volume of water injected upstream in the shale sample with time is monitored (few tenths of millilitres over few weeks).

sedimentation environment of the Goldwyer and Bongabinni shale formations.

Initial re-saturation of the samples was performed by imposing an upstream fluid pressure of $P_P^U = 10$ MPa for up to 10 d while monitoring the fluid pressure at the downstream end of the specimen (large volume reservoir, see Fig. 1a). At the initial stage of the re-saturation process, the downstream reservoir (top end of the specimen) was filled with the simulated pore fluid at room pressure. It then experienced an increase in fluid pressure to reach 10 MPa,

equalling the pressure imposed upstream (bottom end of the sample). This procedure ensures the effective saturation of the specimen with the simulated pore fluid.

Following the saturation stage, the downstream pressure was maintained at $P_P^D = 10$ MPa (reservoir). The upstream pressure was suddenly increased from $P_P^U = 10$ MPa to $P_P^U = 15$ MPa and maintained at that value using a high accuracy volumetric pump (*DigiFlow*™). The difference in fluid pressure between the upstream and downstream ends of the sample was therefore held constant at $\Delta P_P = P_P^U - P_P^D = 5$ MPa throughout the test. In order to maintain the $P_P^U = 15$ MPa in the upstream circuit, the pump adjusts the rate of fluid injection into the specimen. This pump allows for an accurate measurement and a stable displacement of the injection piston for few tenths of millilitres over few weeks.

Once a steady flow was achieved (volume injected depends linearly on time, see Fig. 1b), the constant injection rate imposed by the pump was used to compute the specimen's permeability using Darcy's law, that is,

$$Q = A\frac{k}{\eta}\frac{\Delta P_P}{L} \Rightarrow k = \frac{\mu Q L}{A \Delta P_P},$$

where Q is the pump's steady-state injection rate in (m^3 s^{-1}), k is the sought permeability in (m^2), η is the fluid dynamic viscosity (equal to 10^{-3} Pa s for water at room conditions), ΔP_P is the difference in fluid pressure across the specimen in (Pa), A is the cross-sectional area of the cylindrical specimen in (m^2) and L is its length in (m).

3.3 Frequency-dependent attenuation measurements

Direct attenuation tests were performed in the rock deformation laboratory of ETH-Zurich using the new experimental apparatus described by Madonna & Tisato (2013). Tests were conducted applying small sinusoidal oscillatory stress (10^{-2}–10^2 Hz) and measuring the strain of the cylindrical sample (60 mm in length and 25.4 mm in diameter) with respect to aluminium standard in line with the tested plug. The method employs linear variable differential transformer (LVDT) to measure a bulk strain, by recording the displacement across the whole sample.

The current operating system (Fig. 2a) comprises three main elements. A piezo-electric stack actuator (PZA) generates the sinusoidal axial compressive stress. Two displacement measurement modules consist of linear variable differential transformers. The LVDTs measure the compression and extension displacement of both the sample and the elastic standard with a nanometric resolution. The displacement across the elastic standard is the reference signal to which we compare the displacement across the sample for any phase shift induced by anelasticity (Fig. 2b).

Assuming that the rock behaves as a linear time invariant system, the attenuation factor Q^{-1} is equal to the tangent of the phase shift between the input and the output signal as shown in eq. (7) (e.g. Nowick & Berry 1972; O'Connell & Budiansky 1978; Jackson & Paterson 1987)

$$Q^{-1} = \frac{\Delta E}{2\pi E} = \tan|\theta|, \tag{7}$$

where θ is the phase shift in radians, ΔE is the energy loss during each stress–strain cycle and E is the energy introduced into the rock. The phase shift is calculated by the difference between the input and output signals' phases obtained using the Fourier transform.

Preserved samples cored with different orientation with respect to the bedding were prepared and tested first in their saturated state and then dried in the oven at 105 °C for 24 hr to assess the effect of partial saturation and of anisotropy on attenuation. During attenuation measurements samples were sealed on their cylindrical surface using several layers of cling film to minimize water evaporation during testing. This procedure was tested against measurements of weight before and after the experiments and was found to give satisfactory results.

Due to the prototype nature of the experimental apparatus no absolute displacement calibration could be performed as the displacement signals were not amplified exactly with the same factor between different tests. Hence, it was not possible to calculate Young's modulus and compare it between tests. Nevertheless, before each test a relative calibration was performed to be sure that the strain applied to the samples was between 10^{-6} and 10^{-7}. The accuracy of the experimental apparatus in terms of attenuation values for benchmark samples is discussed in Madonna & Tisato (2013).

Following Madonna & Tisato (2013) we estimated the uncertainty of our measurements based on the statistical error recorded during a test with two aluminium plugs in series within the apparatus. With such a configuration the expected phase shift between the two plugs is zero; however during the test the maximum spread of data recorded amounts to 9.57×10^{-3} rad, and this value is used as the amplitude of error bars around our measurements (see Fig. 8)

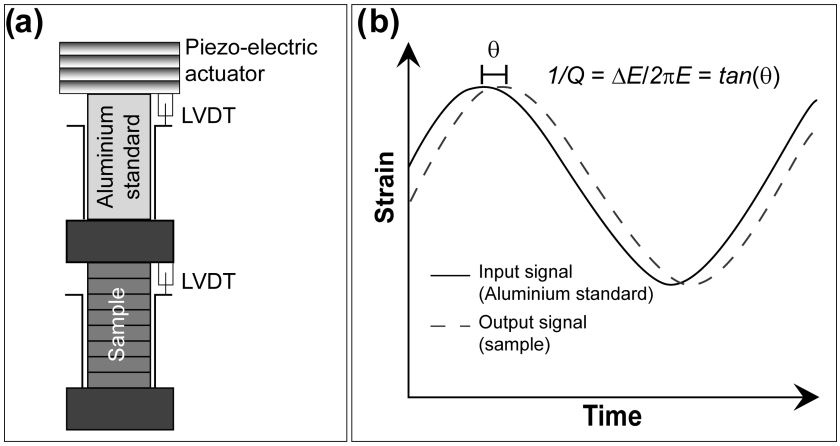

Figure 2. (a) Schematics of the experimental set up for the measurements of frequency dependent attenuation. (b) Conceptual sketch of the experimental measurements: see text for details.

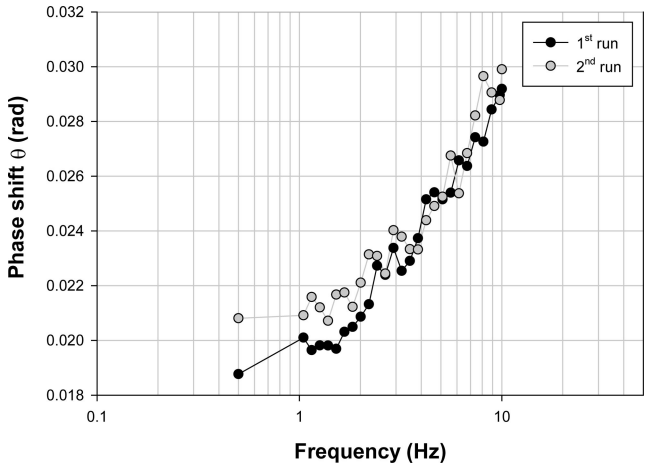

Figure 3. Reproducibility test run on a sample of Goldwyer shale. The experiment was repeated twice on the same specimen removing it and re-installing it in the experimental apparatus after the first measurement cycle. Maximum difference between the two tests amounts to approximately 10 per cent at the lower end of the frequency range.

There are other factors that may induce spurious results such as miscentering of the loading piston with respect to the sample axis or slight lack of parallelism between the flat end surfaces of the cylindrical specimen. These factors may induce a flexural loading and alter the strain measurement on the LVDT, and may results in anomalous phase shift recordings.

The above mentioned artefacts can be recognised as 'jerky' fluctuations of the phase lag when plotted in the frequency domain and can be easily discarded from the recorded data set.

To check the reproducibility of the experimental results we run a broad frequency attenuation test twice on the same sample from the Goldwyer formation. The tested plug was removed from the experimental set-up at the end of the first frequency sweep and then measured again over a limited frequency range. This procedure was mainly aimed at checking that the alignment during sample set up in the attenuation module was accurate enough to give reproducible results as was already verified for simpler standard material (i.e. aluminium, and Berea sandstone and PMMA by Madonna & Tisato 2013).

The tests were performed at room conditions (i.e. no confining pressure applied to the samples), while ultrasonic and geomechanical data collected at high pressure on the same rock types are reported in Delle Piane *et al.* (2011b,c).

The outcome of the test is reported in Fig. 3. The measured phase shift angle θ between the sample and aluminium standard for the first and the second test is plotted against frequency. There is generally an excellent overlap in the data recorded during the two runs, except at the lower frequencies where a greater mismatch is observed. The maximum difference between the two tests amounts to a value of 2.04×10^{-3} rad, corresponding to approximately 10 per cent.

4 RESULTS

4.1 Sample description

The whole cores were CT-scanned and imaged as received, that is, still in plastic liners filled with preserving oil. The Bongabinni Formation core appears as a homogeneous dense material with no evident sedimentary features (Fig. 4). The Goldwyer Formation core shows thin laminations oriented normal to the core axis which can

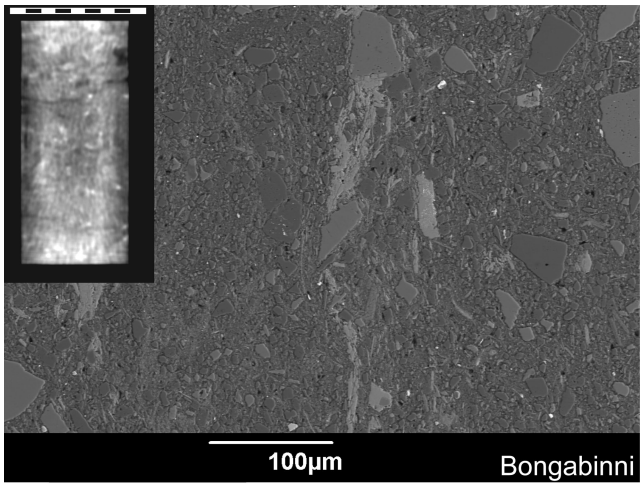

Figure 4. Bongabinni Formation microstructure as observed from the CT scan of a core plug (insert, scale bar is 38 mm); and scanning electron microscope (SEM).

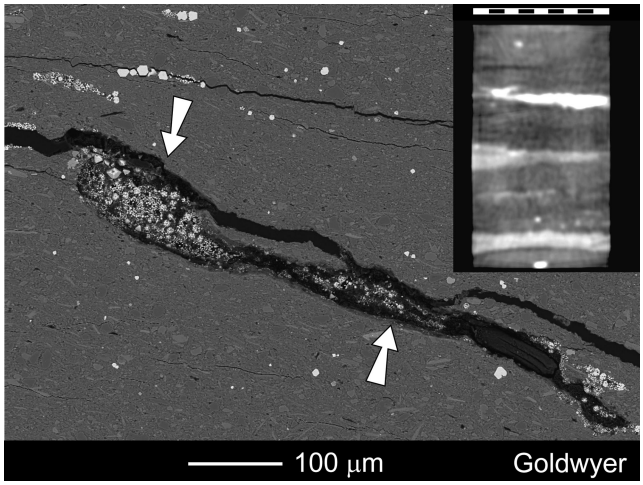

Figure 5. Goldwyer Formation microstructure as observed from the CT scan of a core plug (insert, scale bar is 38 mm); and SEM. Note the sedimentary lamination at the core scale with plane of bedding oriented normal to the sample axis. White arrows indicated material precipitated in the fracture and partially filling it, indicating it may have been at least partially open under in-situ conditions.

be identified as sedimentary planes (Fig. 5). CT scans of individual specimens obtained from these cores highlight how the Goldwyer Formation is composed of heterogeneous material with structures repeated at the centimetre scale.

Scanning electron microscope (SEM) images of thin sections show a very tight grain arrangement for the Bongabinni samples with angular clasts of several tens of microns in size and clusters of needle-shaped anhydrite crystals floating in an ultrafine grained clay matrix; no pervasive porosity can be observed at the SEM scale (Fig. 4), but some isolated, equant, micron-sized pores are detected at the contacts between silt-sized clasts.

The Goldwyer sample appears as a highly laminated sediment comprising thin strata of clay-rich minerals alternating with coarse grained, cemented silt layers. The orientation of these alternating laminae and of the elongated phyllosilicates defines the bedding. Thin elongated fractures run parallel to the bedding and at times are partially filled with pyrite and organic matter (Fig. 5). Mineral associations in the silty layers include quartz, orthoclase, pyrite and

Table 1. Quantitative X-ray diffraction data for the six shale specimens separated by particle size. Qz, quartz; Chl, chlorite; Mica/Ill, mica illite; Ab, albite; Orth, orthoclase; Calc, calcite; Dol, dolomite; Pyr, pyrite; Hem, hematite; Anh, anhydrite.

Formation	Qz	Chl	Mica/Ill	Ab	Orth	Calc	Dol	Pyr	Hem	Anh	
Bongabinni	14	1	41	<1	5		29		1	9	Bulk
Goldwyer	25	4	56	1	6	8		1			
Bongabinni	3	1	92		1				2		0.2–2 μm fraction
Goldwyer	6	5	84		5			<1			
Bongabinni	1	2	97								<0.2 μm fraction
Goldwyer		3	97								

Table 2. Particle size distribution (wt%) and physical properties of the Canning Basin shales. Loss is mainly due to dissolution of carbonates during sample preparation for XRD. CEC, cation exchange capacity; w, water content (wt%); ρ_b, bulk density; ϕ, porosity (by water evaporation); ϕ_{Hg}, porosity by mercury injection.

Formation	<0.2 μm (wt%)	0.2–2 μm (wt%)	>2 μm (wt%)	Loss (wt%)	w (wt%)	ρ_b (g cm^{-3})	ϕ (per cent)	ϕ_{Hg} (per cent)
Bongabinni	7.7	0.8	81.0	10.4	3.8	2.6	9.5	5.7
Goldwyer	10.8	33.5	50.5	5.3	4.6	2.6	11.3	3.6

minor rutile; calcite is also present as intragranular cement reducing the primary porosity; the clay rich layers are mainly composed of ultrafine grained illite and mica with occasional chlorite.

4.2 Mineralogy

4.2.1 Bongabinni formation

The cores appear red in colour with streaks of greenish reduced material. There is no evidence of macroscopic bedding or pervasive fractures at the core scale.

Major mineralogical components are illite/mica and dolomite, with subordinate quartz and anhydrite (Table 1). Minor amounts of disseminated hematite are responsible for the red colour. The fine-grained fraction of the sediment is dominated by illite/mica with sporadic occurrence of orthoclase and chlorite. A significant portion of material is lost during sample preparation for XRD analyses, and is thought to be mainly of carbonate composition. Particle size distribution indicates that the sediment is mainly composed of grains larger than 2 μm. The clay content sums up to 42 per cent while the clay fraction is 19 per cent (Table 1).

4.2.2 Goldwyer formation

The cores appear dark green to greyish in colour, they show very fine lamination down to the millimetre scale and due to their fissile nature require particular handling care.

Quantitative XRD analyses reveal that illite is the dominant phase with abundant quartz and subordinate calcite, chlorite and orthoclase. Subordinate calcite occurs with content ranging between 1 and 8 per cent, and pyrite is also observed. The fine-grained fraction is illite/mica-dominated with chlorite as a second constituent. 50 per cent in weight of the sediments is constituted of particles larger than 2 μm. The clay content is 60 per cent and the clay fraction is 50 per cent (Tables 1 and 2).

4.3 Porosity and water content

The results shown in Fig. 6 were obtained from tests where mercury was injected normal to the macroscopic bedding. Both the Bongabinni and Goldwyer formations show a unimodal pore size

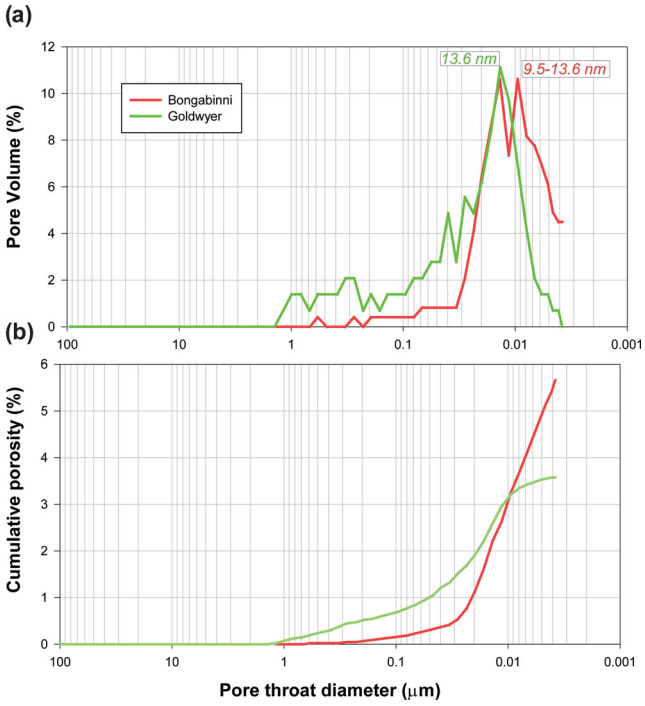

Figure 6. Results of mercury injection porosimetry on the two shale formation from the Canning Basin. (a) Pore volume as a function of pore throat diameter: both samples show modal pore size with a peak around 13.6 nm. The Goldwyer sample displays a slightly broad distribution of pore sizes than the Bongabinni one. (b) Cumulative porosity as a function of pore throat diameter: note that the Goldwyer sample reached full Hg saturation, while the Bongabinni one does not show a flattening of the curve indicating that Hg could not intrude the smallest part of the pore size fraction.

distribution: the former is dominated by pores in the range of 5–15 nm; while the latter shows slightly broader pore size distribution with modal size at around 15 nm. The interconnected porosity measured by mercury injection is 5.7 and 3.6 per cent for the Bongabinni and the Goldwyer samples, respectively. While full Hg saturation was attained in the Goldwyer sample as testified by the plateau in the cumulative porosity versus pore throat diameter curve, the Bongabinni specimen did not reach this stage implying that the reported value of 5.7 per cent likely underestimates the total

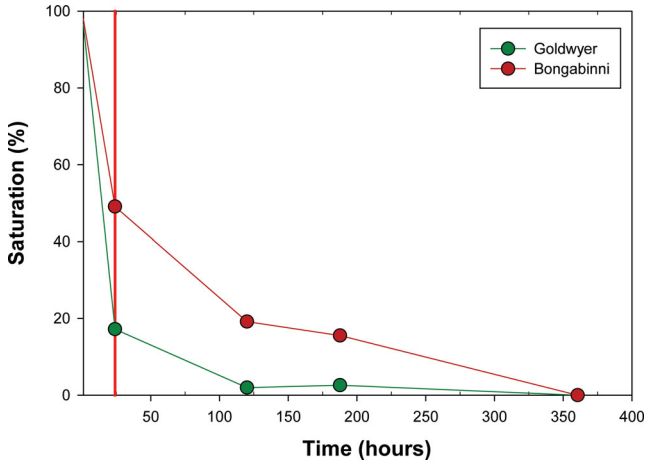

Figure 7. Desaturating curves of the Goldwyer and Bongabinni formations. Saturation is plotted against time spent in the oven at 105 °C. The curves are based on weight measurements taken after suitable thermal equilibration of the samples under vacuum. Note that while the Goldwyer is completely dry after approximately 120 hr, the Bongabinni Formation is still partially saturated even after 300 hr at high temperature. The red vertical line indicates the point in time at which the second attenuation test was performed on the samples (see text).

Table 3. Details of the conditions and results of the permeability tests.

Formation	T (°C)	D (mm)	L (mm)	k (10^{-21} m^2 = nD)
Goldwyer	22.0 ± 0.2	25.31	10.36	4.0
Bongabinni	22.2 ± 0.4	25.24	11.26	43

interconnected porosity. The non-measurable porosity must be constituted by extremely small pore throats that mercury, acting as a non-wetting fluid, is not capable of penetrating even at the highest intrusion pressure of 413 MPa.

In both formations total porosity measured by water evaporation is significantly higher than the interconnected porosity measured by mercury injection and attains values of 9.5 and 11.3 per cent for the Bongabinni and Goldwyer formations, respectively. The outcomes of the drying experiments for the two shales are reported in Fig. 7 in terms of saturation versus time. This test assumes that the preserved samples were fully saturated before the drying process is started. The drying test indicates that the Goldwyer Formation de-saturates significantly faster than the Bongabinni. This observation seems consistent with the mercury porosimetry results which showed that the dominant pore throat diameter in the Goldwyer formation is larger than in the Bongabinni formation.

4.4 Permeability measurements

Table 3 shows the details of the testing conditions for each sample along with the results in terms of water permeability.

4.5 Attenuation measurements

While it was possible to measure attenuation on two orthogonally cored specimens of the Bongabinni formation; only one vertical core plug from the Goldwyer Formation could be cored and tested. The output of the direct attenuation measurements are plotted in Fig. 8. Each sample was first tested in its preserved state (Fig. 8a), then in a partially saturated state after drying in an oven at 105 °C for 24 hr (Fig. 8b). Therefore, three samples in total were tested.

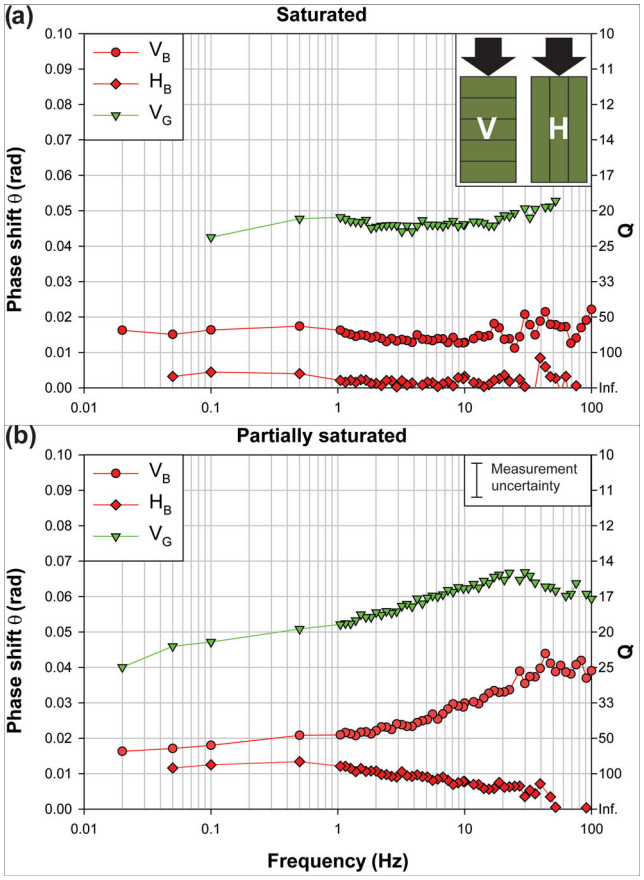

Figure 8. Results of the experimental measurements of frequency dependent attenuation: (a) results obtained on the preserved samples with native fluid content; (b) results obtained on the partially saturated samples after drying in the oven at 105 °C for 24 hr.

In its preserved state (Fig. 8a), assumed fully water-saturated, vertical sample V_G (Goldwyer cored normal to bedding) displays the lowest quality factor Q (highest attenuation Q^{-1}) among the three samples, with values of $Q \simeq 20$. Of the two twin Bongabinni samples the horizontal one cored parallel to the bedding and labelled H_B has the highest quality factor (lowest attenuation) with values of $Q > 100$. In contrast, the vertical twin sample V_B (Bongabinni cored normal to bedding) displays Q values of $Q \simeq 70-80$, indicating an anisotropy of the quality factor. All three samples qualitatively show no trend in the frequency dependency of the quality factor Q or attenuation. Some scatter in the data is observed at frequencies higher than 20 Hz: this is thought to be due to small resonance of the apparatus influencing the measurements.

Measurements collected on the partially saturated vertical sample V_G (Fig. 8b) show a broad asymmetric bell shape with a minimum in quality factor Q (peak in attenuation) at $f \approx 30$ Hz. The quality factor is significantly lower in this situation than in the water-saturated condition. The Bongabinni sample cored normal to bedding V_B also displays an asymmetric bell-shaped curve with peak in attenuation at $f \approx 42$ Hz. The change in quality factor as a function of frequency seems steeper than that observed for sample V_G.

The partially saturated sample H_B (Bongabinni cored parallel to bedding) displays a modest frequency dependency with a quality factor Q slightly increasing at the high end of the tested frequency range.

Over all, the data for all samples indicate that the quality factor Q is higher (lower attenuation) in the saturated state than in the

Table 4. Material parameters used for the identification of the dominant attenuation mechanism: ϕ, porosity; η, viscosity of the pore fluid; ρ_{fl}, density of the pore fluid; k, permeability; E_u, saturated undrained Young's modulus; K_u, saturated undrained bulk modulus calculated from E_u and using an assumed Poisson's ratio of 0.3.

Formation	ϕ (%)	η (Pa s^{-1})	ρ_{fl} (kg m^{-3})	k (10^{-21} m^2 = nD)	E_u (GPa)	K_u (GPa)
Bongabinni	9.5	10^{-3}	10^3	43.0	6.9	5.8
Goldwyer	11.3	10^{-3}	10^3	4.0	4.2	3.5

partially saturated state. Moreover, the frequency dependency of the quality factor seems to be significant only in the partially saturated state.

5 DISCUSSION

This section discusses (1) the possible sources of attenuation in the tested specimens and (2) the correlations between elastic, mechanical and attenuation anisotropies in shales.

5.1 Attenuation mechanisms

An important cause of attenuation/dispersion of seismic waves propagating in rocks is the presence of fluids in the pore space and their physical interactions with the rock's solid frame. The ability of a fluid to move within the connected porosity is controlled by the frequency of the wave. In the high frequency limit, the fluid has no time to move following pressure gradients induced by the propagating wave. In contrast, in the low frequency limit, fluid has the time to flow until pore pressure is equilibrated (uniform) at all scales. Between these two limiting situations several attenuation/dispersion mechanisms can be triggered depending on the frequency of the propagating wave, the microstructure of the rock, the boundary conditions and the scale of heterogeneities (Winkler & Murphy 1995; Muller *et al.* 2010; Sarout 2012).

Our analysis is based on the physical parameters characterizing the Bongabinni and Goldwyer formations samples reported in Table 4 and focuses on the following mechanisms already identified in the literature:

(1) Fluid diffusion in the pore space at the meso- or macroscopic scale.
(2) Transition from viscous flow of fluid to inertial drag between solid matrix and pore fluid (macroscopic scale).
(3) Squirt-flow between different pore types (microscopic scale).

5.1.1 Macroscopic diffusion in water-saturated shales

Dimensional analysis of diffusion processes reveals that a diffusion coefficient D (in m^2 s^{-1}) is proportional to a squared characteristic length L^2 and inversely proportional to a characteristic relaxation time $\tau_d = 1/f_d$.

$$D \approx \tau_d L^2 = \frac{1}{f_d} L^2. \tag{8}$$

This is the fundamental relation for the estimation of the cut-off frequencies associated with attenuation/dispersion due to fluid motion in the pore space and it is based on the assumption that a representative volume element exists such that diffusion occurs across such volume in a continuous media (Cleary 1978). The diffusion coefficient is well defined for fully saturated porous media (see for example, Wang 2000) and is related to the permeability of the porous rock k (in m^2), to the fluid dynamic viscosity η (in Pa s^{-1}) and to the rock bulk modulus K (in Pa),

$$D \approx \frac{k}{\eta} K_u. \tag{9}$$

Two situations can be distinguished when stress perturbations are passing through rocks: the drained regime and the undrained regime, each corresponding to a specific bulk modulus. In the drained regime the fluid has time to flow in response to a stress perturbation (extremely low frequency). No pore pressure changes are expected and the fluid does not contribute to the overall stiffness of the rock, therefore the drained and dry bulk moduli coincide $K_d = K_{dry}$. In the undrained regime the fluid does not have enough time to flow, that is, its mass and volume are constant within a given volume of rock subject to a stress perturbation and contributes to the overall stiffness of the rock and the corresponding undrained bulk modulus $K_u > K_d$.

The cut-off frequency separating the drained and the undrained regimes (f_d) can be estimated combining eqs (8) and (9)

$$f_d \approx \frac{k}{\eta} \frac{K_u}{L^2}, \tag{10}$$

where f_d can be compared to the frequency range explored in the experiments reported above (10^{-2} to 10^2 Hz) using the data available in Table 4 and the samples dimensions (60 mm in length and 25.4 mm in diameter). Using eq. (10) with L equal to the half-length (axial diffusion) or to the radius (radial diffusion) of the samples, estimated values of f_d in the fully saturated samples are between $f_d = 2.7 \times 10^{-4}$ and 1.5×10^{-3} Hz for the Bongabinni Formation samples; and between $f_d = 1.6 \times 10^{-5}$ and 8.7×10^{-5} Hz for the Goldwyer Formation sample. Therefore the attenuation associated with diffusion across the water-saturated samples is expected to occur at frequencies much lower than those explored in the experiments, consistent with the lack of attenuation peak measured during the tests (Fig. 8a). The water-saturated samples are effectively tested in the undrained regime and no macroscopic flow occurs. Note that f_d also corresponds to the cut-off frequency associated with the 'artificial attenuation' caused by the experiment open-pore boundary condition as extensively described by Dunn (1986).

5.1.2 Macroscopic interactions: diffusive-inertial transition

In a water-saturated rock, at frequencies higher than f_d, inertial effects are expected, mainly due to the difference in density between the fluid and solid phases. This phenomenon is predicted by Biot's theory of poroelasticity (Biot 1962): the cut-off frequency associated with the transition between the quasi-static (Gassmann limit) and the dynamic (inertial) domains is called Biot's frequency f_B. Around f_B, viscous and drag forces are of comparable magnitude and peak attenuation associated with this transition is expected. This frequency can be expressed as

$$f_B = \frac{\phi \eta}{2\pi \rho_{fl} k}. \tag{11}$$

Using the parameters reported in Table 4, $f_B = 3.5 \times 10^{11}$ Hz and $f_B = 4.5 \times 10^{12}$ Hz for the Bongabinni and Goldwyer formations, respectively. The attenuation peak associated with this transition is outside the experimental frequency range explored in this study. This also implies that the samples tested in range $f = 10^{-2}$ to 10^2 Hz in the laboratory lie in the viscous flow regime.

5.1.3 Mesoscopic diffusion

Mesocale defines features in the rock that have a characteristic length sale (size and/or spacing) L_m smaller than the size of the sample, yet larger than the characteristic size of the fluid bearing features that constitute the rock microstructure.

Eq. (10) can be used to relate the cut-off frequency f_d associated with an attenuation mechanism in the partially saturated shale samples (Fig. 8b) to the mesoscale diffusion length L_m and the parameters reported in Table 4. However, since the bulk modulus of the shales in this partially saturated situation is not available, K_u is used instead. This is a reasonable approximation since the bulk modulus of the shales in the partially saturated situation is not expected to be different from K_u by orders of magnitude. Inverting eq. (10) for L_m using the peak attenuation frequencies measured during the tests on the partially saturated samples (Fig. 8b) yields the characteristic length $L_m = 77$ and 22 μm for the Bongabinni and the Goldwyer vertical samples, respectively (Fig. 9a).

These values are analysed in relation to the possible existence of (1) fluid saturation patches (Dvorkin & Nur 1998; Johnson 2001) and (2) mesoscopic fractures (Pride & Berryman 2003).

Patchy saturation refers to a heterogeneous spatial distribution of fluids in the pore space, that is, the existence of several patches where one fluid saturates the pore space, while the remaining volume is saturated with another fluid (e.g. water and air). Fluid motion in such a medium can be responsible for the observed attenuation if (1) the wavelength of the stress perturbation is much larger than a representative volume element and (2) if the patches are much larger than the characteristic pore size.

A characteristic patch size of $L_m = 77$ and 22 μm for the Bongabinni and the Goldwyer vertical samples, respectively indicates that the estimated patches sizes are much larger than the modal pore size (14 nm) obtained from the mercury injection tests on sub-samples of the two shales. The ultrasonic wave velocities measured on these shales (Delle Piane *et al.* 2011c) yield a wavelength of the order of few millimetres. Therefore in the frequency range of stress perturbations applied in the present oscillation experiments (10^{-2} to 10^2 Hz), the wavelength is even larger so that the saturation patches are also much smaller than this wavelength. These two observations support the patchy saturation mechanism as a possible cause of the observed attenuation peaks in the partially saturated shales investigated.

The existence of mesoscopic fractures with a characteristic size/spacing larger than the modal pore size (14 nm) of the two shales can also be responsible for the observed attenuation peaks. If such fractures are filled with water and are deformed by the applied stress perturbation, water can diffuse into the surrounding porous material containing much smaller pores, cracks, grain contacts, and/or pore throats. The relevant characteristic diffusion length is then the average half-distance between such fractures. Using eq. (10) yields a fractures' average half-spacing $L_m = 77$ and 22 μm for the Bongabinni and the Goldwyer vertical samples, respectively. In Fig. 4 (Bongabinni Formation shale), no mesoscale fracture can be observed, despite the relatively wide field of view of the SEM image. Therefore water diffusion out of mesoscale fractures is not a likely mechanism for explaining the attenuation peak observed in the Bongabinni Formation shale.

In Fig. 5 (Goldwyer Formation), mesoscale fractures are visible and a half-spacing between them of the order of $L_m = 22$ μm seems reasonable. However, it is likely that these fractures are the result of sample handling and preparation. If these fractures exist in the

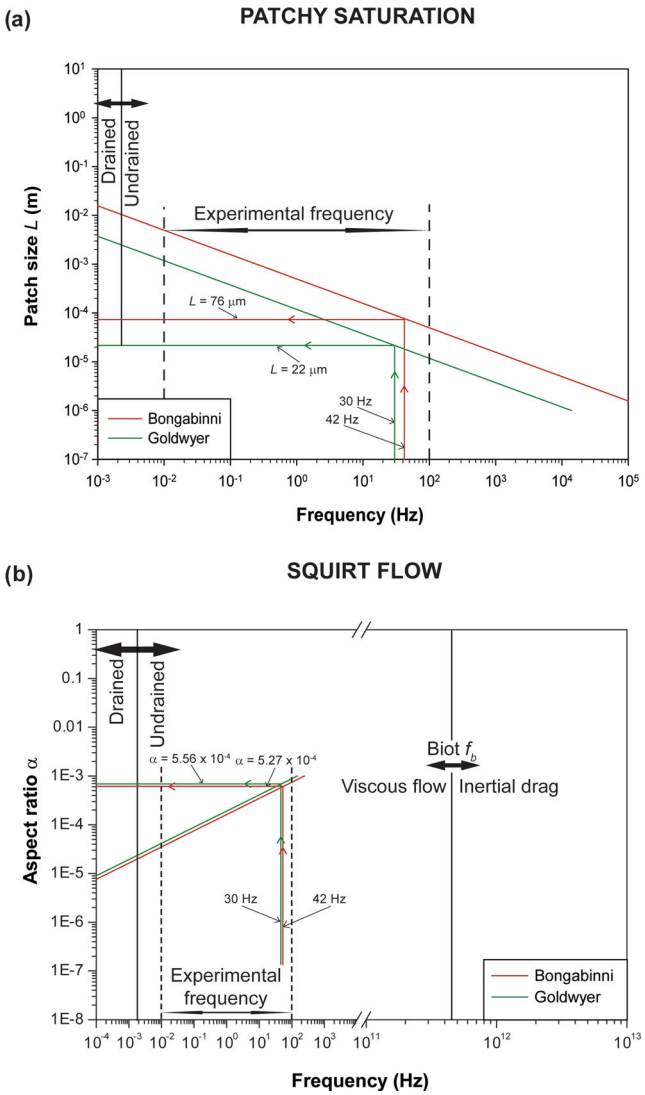

Figure 9. Inversion of the experimental results according to two of the attenuation mechanisms discussed in the text. (a) Mesoscopic fluid flow associated with the patchy saturation mechanism: the inclined lines are calculated using eq. (10) and the rock specific values reported in Table 4; vertical reference frequencies for the Goldwyer and Bongabinni samples correspond to the attenuation peaks identified during the tests under partial saturation state and reported in Fig. 8(b); horizontal lines indicate the patch size (L) inverted from eq. (10). The transition between drained and undrained fields corresponds to the characteristic frequency f_d discussed in the text. (b) Microscopic fluid flow associated with the squirt mechanism: the inclined lines are calculated using eq. (12) and the rock specific values listed in Table 4. Vertical reference frequencies for the Goldwyer and Bongabinni samples correspond to the attenuation peaks identified during the tests under partial saturation state and reported in Fig. 8(b). Horizontal lines indicate the aspect ratio inverted from eq. (12). See text for the definition of Biot's critical frequency f_B.

preserved Goldwyer shale sample, the attenuation peak should also be observed in the preserved sample, which is not the case. On the other hand, if these fractures are artificially induced by the drying process (e.g. due to clays shrinkage), they are most likely dry due to the extremely low permeability of the porous material surrounding the fractures and the large capillary forces keeping water inside the small pores (∼14 nm). Therefore this mesoscale mechanism is not likely to contribute to the attenuation peak observed in the partially saturated Goldwyer Formation test (Fig. 8b).

5.1.4 Microscopic scale: squirt-flow

At the microscopic level, fluid flow can take place between individual pores within any representative volume element. This mechanism is referred to as 'squirt flow' and it is associated with fluid squirting from a stress-sensitive type of pore (e.g. cracks,) into a stiffer one (e.g. equant pore) when a stress perturbation is applied to the rock.

Squirt flow attenuation peak occurs at a frequency f_s related to the geometry of the stress-sensitive type of pores (their aspect ratio). Several authors provided estimates of this cut-off frequency and most of them bear the same dependency of f_s to the cubed aspect ratio of the pores, although there are some differences regarding the elastic modulus used in the calculation. Following Le Ravalec & Gueguen (1996) or Sarout (2012), f_s can be approximated by

$$f_s \approx \frac{\alpha^3 E_0}{24\eta}, \tag{12}$$

where α is the aspect ratio of the compliant pore and E_0 is the Young's modulus of the solid medium in which a single compliant pore is embedded.

Solving eq. (12) for α using the parameters listed in Table 4, and the peak frequencies obtained on the partially saturated samples, one can derive a characteristic pore geometry expressed as an aspect ratio $\alpha \sim 5 \times 10^{-4}$ (Fig. 9b). Such a value is consistent with the ones reported by other authors as inverted from ultrasonic tests, dipole wireline log investigations and low frequency laboratory experiments (e.g. Jones 1986; Bayuk *et al.* 2008; Angus *et al.* 2009) and numerical simulations (Mavko & Nur 1979; Palmer & Traviolia 1980).

On the other hand, if squirt-flow is to contribute significantly to the attenuation peak observed in the partially saturated shales, it is expected to induce an attenuation peak in the preserved shale samples as well, which is not the case. This rationale is valid only if the solid frame of the shales remains unchanged during the drying process but,. as discussed above in the case of mesoscale fractures, shales can be damaged by the drying process itself and microscale cracks be generated in the partially saturated sample that were not initially present in the preserved sample.

Based on the characteristic frequencies associated with five possible wave-induced attenuation mechanisms and on the measured properties of two different shales, mesoscale diffusion associated with patchy saturation is likely to contribute to the attenuation peaks observed in the partially saturated samples of both shales. In contrast, Biot mechanism, mesoscale diffusion associated with fractures and the artificial sample boundary condition effects are not likely to be applicable for both preserved shale samples. It is more difficult to reach a definitive conclusion regarding squirt-flow associated with microscale cracks. The conditions for the microscale squirt-flow to contribute to the observed attenuation peaks in both partially saturated shales without being visible in the preserved shales can be summarized as follows (1) microscale cracks do not truly exist in the preserved samples; (2) they are generated in the partially saturated sample by the drying process. In the partially saturated samples certain microscale cracks can potentially remain filled with water to the same extent as equant pores can; high pressure experiments would be required to discriminate the contribution of compliant cracks to the measured attenuation.

This analysis constitutes a first attempt in improving our understanding of the new experimental data available on shales and provides information about the field of validity of end-member mechanisms. Nevertheless, it seems likely that in the laboratory as well as in field different attenuation mechanisms may be competing with variable relative contributions given that natural rocks and shales in particular present a wide range of pore sizes, shapes and microstructures.

5.2 Attenuation anisotropy

Rock fabric (i.e. minerals and pore space arrangement), can give rise to significant elastic, mechanical and/or permeability anisotropy. As rock fabric and fluid distribution in the pore space control attenuation, it is expected that a macroscopically anisotropic rock will display a directional dependency of the quality factor Q (or attenuation Q^{-1}).

Shales are known to show various degrees of elastic anisotropy and are normally described as transversely anisotropic rocks (e.g. Podio *et al.* 1968; Hornby 1998; Sarout & Guéguen 2008). The samples tested in this study are no exception: dynamic elastic moduli measured on samples of the Bongabinni and Goldwyer from the same parent cores used in this study indicate a significant anisotropy of ultrasonic wave velocities, due to clay particle alignment and presence of bedding parallel thin cracks (Delle Piane *et al.* 2011b,c).

The experimental results collected on the Bongabinni pair of samples indicate that attenuation is higher when low frequency waves propagate across the macroscopic bedding than parallel to it. This observation is in agreement with the ultrasonic measurements of Stanley & Christensen (2001) and of Deng *et al.* (2009); the narrow band measurements of Domnesteanu *et al.* (2002) on saturated shales from the North Sea under over pressured conditions; and the broad band tests of Hofmann (2006) who reported higher losses for oscillations applied along a direction normal to the bedding. Indeed previous studies identified the symmetry axis of shales (normal to symmetry/bedding plane) as the most compliant axis from the elastic point of view suggesting an analogy with the attenuation case.

Anisotropy of attenuation is consistently seen in both the saturated and the partially saturated situations and in both experiments sample H_B (Bongabinni horizontal) shows negligible frequency dependency as opposed to the two vertically cored samples. Planar discontinuities tend to be aligned with the macroscopic bedding and have high compliance when compared to the surrounding porous material. An oscillatory stress perturbation travelling normal to the short axis of these discontinuities will cause them to close and open alternatively; the relatively impermeable walls of the discontinuities being squeezed together will induce a fluid pressure gradients resulting in fluid movements toward regions of lower pressures. In the opposite situation for which a stress perturbation is travelling along the macroscopic bedding, virtually no load transfer occurs between the solid framework and the fluid located in the elongated discontinuities, thus fluid motion is relatively limited.

6 CONCLUSIONS

Experimental measurements of attenuation were collected on samples of two shale formations in the frequency range 0.01–100 Hz. Experiments were designed to assess the role of saturation and anisotropy on attenuation by repeating the measurements first on samples with their preserved native fluid content, and then following dehydration in an oven at 105 °C for 24 hr.

Results indicate that both shale types show some degree of attenuation with the highest values recorded normal to the macroscopic bedding. Moreover no frequency dependency is observed in the preserved samples within the range of frequencies explored in this study. On the other hand partially saturated samples show peaks in attenuation at around 40 Hz when the stress perturbation is transmitted normal to the macroscopic bedding. We interpret this behaviour to be due to fluid motion at the meso- and microscale; that is, a combination of (1) mesoscale fluid diffusion around saturated patches of the samples; (2) microscale squirt-flow between compliant pores (cracks, grain contacts) and neighbour cavities, either non-coplanar compliant pores or stiffer equant pores; and possibly (3) mesoscale fluid diffusion from fractures into the surrounding porous material in one of the two shale samples.

This interpretation is compatible with microstructural investigation by SEM and mercury injection revealing both quantitative and qualitative information on the pore geometry and size within the two shales.

ACKNOWLEDGEMENTS

We wish to dedicate this contribution to the late Luigi Burlini. We thank Nicola Tisato and Robert Hoffman for their contribution to the development of the experimental apparatus. Tobias Muller and Beatriz Quintal are thanked for several stimulating discussions.

The Australian Academy of Science supported part of the research trough a travel grant to CDP. Samples were kindly provided by A. Mory (Geological Survey of Western Australia). Ian Jackson and an anonymous reviewer are thanked for their comments and critical reading of the manuscript.

REFERENCES

Adam, L., Batzle, M. & Brevik, I., 2006. Gassmann's fluid substitution and shear modulus variability in carbonates at laboratory seismic and ultrasonic frequencies, *Geophysics,* **71**(6), F173–183.

Adelinet, M., Fortin, J, Gueguen, Y., Schubnel, A. & Geoffroy, L., 2010. Frequency and fluid effects on elastic properties of basalt: experimental investigations, *Geophys. Res. Lett.,* **37,** L02303, doi:10.1029/2009gl041660.

Allen, J.L. & Peddy, C.P., 1993. *Amplitude Variation with Offset: Gulf Coast Case Studies*, Society of Exploration Geophysicists, 126 pp.

Angus, D.A., Verdon, J.P., Fisher, Q.J. & Kendall, J.M., 2009. Exploring trends in microcrack properties of sedimentary rocks: an audit of dry-core velocity-stress measurements, *Geophysics,* **74,** E193–E203.

Batzle, M.L., Han, D. & Hofmann, R., 2006. Fluid mobility and frequency-dependent seismic velocity—direct measurements, *Geophysics,* **71**(1), N1–N9.

Bayuk, I.O., Ammerman, M. & Chesnokov, E.M., 2008. Upscaling of elastic properties of anisotropic sedimentary rocks, *Geophys. J. Int.,* **172**(2), 842–860.

Biot, M.A., 1962. Mechanics of deformation and acoustic propagation in porous media, *J. appl. Phys.,* **33**(4), 1482–1498.

Boisson, J.Y., Bertrand, L., Heitz, J.F. & Golvan, Y., 2001. In situ and laboratory investigations of fluid flow through an argillaceous formation at different scales of space and time, Tournemire tunnel, southern France, *Hydrogeol. J.,* **9**(1), 108–123.

Brace, W.F., 1980. Permeability of crystalline and argillaceous rocks, *Int. J. Rock Mech. Min. Sci. Geomech. Abstr.,* **17,** 241–245.

Carpenter, E.W. & Flinn, E.A., 1965. Attenuation of teleseismic body waves, *Nature,* **207**(4998), 745–746.

Cleary, M.P., 1978. Elastic and dynamic response regimes of fluid-impregnated solids with diverse microstructures, *Int. J. Solids Struct.,* **14**(10), 795–819.

Delle Piane, C., Dewhurst, D.N., Siggins, A.F. & Raven, M.D., 2011a. Stress-induced anisotropy in brine saturated shale, *Geophys. J. Int.* **184**(2), 897–906.

Delle Piane, C., Almqvist, B., Raven, M. & Dewhurst, D., 2011b. Shale anisotropy: linking mineral fabric and elastic properties, in *Proceedings of the Euroconference on Rock Physics and Geomechanics,* 17–21 October, Trondheim, Norway.

Delle Piane, C., Esteban, L., Dewhurst, D., Clennell, B. & Raven, M., 2011c. Rock physics and petrophysics testing of shales from the Canning Basin, Western Australia, *SEG Tech. Prog. Expanded Abstracts,* **30**(1), 2135–2139.

Deng, J., Wang, S. & Han, D.H., 2009. The velocity and attenuation anisotropy of shale at ultrasonic frequency, *J. Geophys. Eng.,* **6**(3), 269–278.

Domnesteanu, P., McCann, C. & Sothcott, J., 2002. Velocity anisotropy and attenuation of shale in under- and overpressured conditions, *Geophys. Prospect.,* **50**(5), 487–503.

Dunn, K.-J., 1986. Acoustic attenuation in fluid-saturated porous cylinders at low frequencies, *J. acoust. Soc. Am.,* **79,** 1709–1721.

Dvorkin, J. & Nur, A., 1998. Acoustic signature of patchy saturation, *Int. J. Solids Struct.,* **34–35,** 4803–4810.

Ghorbani, A., Zamora, M. & Cosenza, P., 2009. Effects of desiccation on the elastic wave velocities of clay-rocks, *Int. J. Rock Mech. Min. Sci.,* **46**(8), 1267–1272.

Ghori, K.A.R. & Haines, P.W., 2006. Petroleum geochemistry of the Canning Basin, Western Australia: basic analytical data 2004–05: Western Australia Geological Survey, Record 2006/7.

Haines, P.W., 2004. Depositional facies and regional correlations of the Ordovician Goldwyer and Nita Formations, Canning Basin, Western Australia, with implications for petroleum exploration, Western Australia Geological Survey. Report number 2004/7.

Hofmann, R., 2006. Frequency dependent elastic and anelastic properties of clastic rocks, Colorado School of Mines, *PhD thesis,* 332 pp.

Hornby, B., 1998. Experimental laboratory determination of the dynamic elastic properties of wet, drained shales, *J. geophys. Res.-Solid Earth,* **103**(B12), 29 945–29 964.

Jackson, I. & Paterson, M.S., 1987. Shear modulus and internal friction of calcite rocks at seismic frequencies: pressure, frequency and grain size dependence, *Phys. Earth planet. Inter.,* **45**(4), 349–367.

Johnson, D.L., 2001. Theory of frequency dependent acoustics in patchy-saturated porous media, *J. acoust. Soc. Am.,* **110,** 682–694.

Jones, T.D., 1986. Pore fluids and frequency-dependent wave propagation in rocks, *Geophysics,* **51,** 1939–1953.

Jones, C. & Meredith, P., 1998. An experimental study of elastic wave propagation anisotropy and permeability anisotropy in an illitic shale, *SPE/ISRM Rock Mechanics in Petroleum Engineering*. Paper #47369.

Jurin, J., 1719. An account of some experiments shown before the Royal Society; with an enquiry into the cause of the ascent and suspension of water in capillary tubes, *Trans. R. Soc.,* **30,** 739–747.

Klimentos, T., 1995. Attenuation of P- and S-waves as a method of distinguishing gas and condensate from oil and water, *Geophysics,* **60,** 447–458.

Le Ravalec, M. & Gueguen, Y., 1996. High- and low-frequency elastic moduli for a saturated porous/cracked rock: differential self-consistent and poroelastic theories, *Geophysics,* **61,** 1080–1094.

Madonna, C. & Tisato, N., 2013. Seismic Wave Attenuation Module (SWAM): a tool for laboratory low-frequency seismic attenuation measurements, *Geophys. Prospect.,* **61**(2), 302–314.

Mavko, G. & Nur, A., 1979. Wave attenuation in partially saturated rocks, *Geophysics,* **44**(2), 161–178.

Muller, T.M., Gurevich, B. & Lebedev, M., 2010. Seismic wave attenuation and dispersion resulting from wave-induced flow in porous rocks—a review, *Geophysics,* **75**(5), 75A147–75A164.

Murphy, W.F., 1982. Effects of partial water saturation on attenuation in Massilon sandstone and Vycor porous glass, *J. acoust. Soc. Am.,* **71,** 1458–1468.

Neuzil, C.E., 1994. How permeable are clay sand shales? *Water Resour. Res.,* **30**(2), 145–150.

Nowick, A.S. & Berry, B.S., 1972. *Anelastic Relaxation in Crystalline Solids,* Academic Press.

O'Connell, R.J. & Budiansky, B., 1978. Measures of dissipation in viscoelastic media, *Geophys. Res. Lett.,* **5**(1), 5–8.

Palmer, I.D. & Traviolia, M.L., 1980. Attenuation by squirt flow in undersaturated gas sands, *Geophysics,* **45**(12), 1780–1792.

Podio, A.L., Gregory, A.R. & Gray, K.E., 1968. Dynamic properties of dry and water-saturated Gree River shale under stress, *SPE J.,* **8,** 389–404.

Pride, S.R. & Berryman, J.G., 2003. Linear dynamics of double-porosity dual-permeability materials. I. Governing equations and acoustic attenuation, *Phys. Rev. E,* **68**(3), doi:036603-1-036603-10.

Sarker, R. & Batzle, M., 2010. Anisotropic elastic moduli of the Mancos B Shale – An experimental study, *SEG Tech. Prog. Expanded Abstracts,* **29**(1), 2600–2605.

Sarout, J., 2012. Impact of pore space topology on permeability, cut-off frequencies and validity of wave propagation theories. *Geophys. J. Int.,* **189**(1), 481–492.

Sarout, J. & Guéguen, Y., 2008. Anisotropy of elastic wave velocities in deformed shales, Part 2: modeling results, *Geophysics,* **73**(5), D91–D103.

Spencer, J.W., 1981. Stress Relaxations at low frequencies in fluid-saturated rocks: attenuation and modulus dispersion, *J. geophys. Res.,* **86**(B3), 1803–1812.

Stanley, D. & Christensen, N.I., 2001. Attenuation anisotropy in shale at elevated confining pressures, *Int. J. Rock. Mech. Min. Sci.,* **38**(7), 1047–1056.

Wang, H.F., 2000. *Theory of Linear Poroelasticity with Applications to Geomechanics and Hydrogeology,* Princeton Univ. Press, 276 pp.

Winkler, K.W. & Murphy, W.F. III., 1995. Acoustic velocity and attenuation in porous rocks, in *Rock Physics & Phase Relations: A Handbook of Physical Constants*, AGU Ref. Shelf, Vol. 3, pp. 20–34, ed. Ahrens, T.J., AGU.

Winkler, K.W. & Nur, A., 1982. Seismic attenuation: effects of pore fluids and frictional sliding, *Geophysics,* **47**(1), 2–16.